Title	Formation of three-dimensional dislocation networks in α-iron twist grain boundaries: Insights from first-principles neural network interatomic potentials
Author(s)	Meng, Fan Shun; Li, Jiu Hui; Shinzato, Shuhei et al.
Citation	Computational Materials Science. 2025, 253, p. 113812
Version Type	VoR
URL	https://hdl.handle.net/11094/101388
rights	This article is licensed under a Creative Commons Attribution-NonCommercial-NoDerivatives 4.0 International License.
Note	

Computational Materials Science 253 (2025) 113812

Contents lists available at ScienceDirect

Computational Materials Science

journal homepage: www.elsevier.com/locate/commatsci

Full length article

Formation of three-dimensional dislocation networks in α-iron twist grain boundaries: Insights from first-principles neural network interatomic potentials

Fan-Shun Meng [a,*], Jiu-Hui Li [b], Shuhei Shinzato [a], Kazuki Matsubara [c], Wen-Tong Geng [d], Shigenobu Ogata [a]

[a] *Department of Mechanical Science and Bioengineering, Graduate School of Engineering Science, Osaka University, 1-3 Machikaneyama, Toyonaka, Osaka, 560-8531, Japan*
[b] *School of Science, Liaoning University of Technology, Jinzhou, 121001, China*
[c] *Steel Research Laboratory, JFE Steel Corporation, Kawasaki, 210-0855, Japan*
[d] *Department of Physics, Zhejiang Normal University, Jinhua, 321004, China*

ARTICLE INFO

Dataset link: https://www.ctcms.nist.gov/potentials/entry, https://github.com/mengfsou/FeH-NNIP-ensemble

Keywords:
Twist grain boundary
α-iron
Atomistic simulation
Three-dimensional dislocation network
Density functional theory based neural network interatomic potentials

ABSTRACT

We conducted a systematic analysis of the atomic structure and energy of (001), (110), and (111) twist grain boundaries (TWGBs) in α-iron using a recently developed neural network interatomic potential (NNIP). This study showcases typical dislocation networks within TWGBs that exhibit small twist angles. Notably, we observed a three-dimensional (3D) dislocation network in (111) twist grain boundaries, primarily composed of $\frac{1}{2}\langle 111\rangle$ dislocations—structures unattainable using previously proposed empirical potentials, hence unreported in earlier studies. The novel 3D dislocation network was further validated through several approaches, including principal component analysis (PCA), an NNIP ensemble model, and cross-validation with other machine learning interatomic potentials designed for α-iron. This breakthrough offers a new perspective on the properties of twist grain boundaries, potentially impacting our understanding of their strength, toughness, and mobility.

1. Introduction

Grain boundaries (GBs) are prevalent two-dimensional defects in materials, exerting a profound impact on the mechanical properties of polycrystalline materials. For instance, the refinement of grains can markedly alter the strength and ductility of materials [1] through interactions between GBs and dislocations. Additionally, GBs can act as reservoirs for defects like impurities and vacancies [2–4]. This phenomenon can result in the stabilization of grain boundaries (GBs) structure or, conversely, trigger the initiation of crack embryos at GBs, ultimately leading to fractures. Given its extensive use as a structural material, iron has garnered considerable attention, prompting substantial research into the atomic structure, formation energy of GBs [5–10].

While significant efforts have been dedicated to understanding symmetric tilt GBs (STGBs) in α-iron [5,11,12], the same cannot be said for twist grain boundaries (TWGBs). The square dislocation network pattern in (100) TWGBs [13] and hexagonal dislocation network pattern in (110) TWTBs [14] were experimentally observed decades ago and also have been reproduced in atomistic simulations [15,16]. Nevertheless, the existence and specific morphology of the dislocation network in (111) TWGBs remain ambiguous in both experimental and theoretical contexts. As other body-centered cubic (BCC) metals such as Nb [17], W [18], and Mo [19], the most well-studied TWGBs in α-iron are those terminated with the (110) plane. Yang et al. [16] were pioneers in investigating the structure and energy of (110) TWGBs in α-iron using the molecular statics method in conjunction with an embedded-atom method (EAM) potential. They revealed the presence of a hexagonal dislocation network (HDN) in TWGBs featuring small twist angles and further explored the anisotropic mobility of HDNs in a series of (110) TWGBs subjected to external shear stress [20]. Sarochawikasit et al. [21] fitted Read–Shockley–Wolf and parabolic functions to predict the STGBs and TWGBs energies based on data obtained using empirical interatomic potentials (EIPs). However, they did not address the atomic configurations of TWGBs. Other researchers, such as Liu et al. [22], Wang et al. [12], and Wakeda et al. [23], have examined stability and grain boundary energy for specific TWGBs, respectively. However, a

---

* Corresponding author.
E-mail address: fanshun.meng@tsme.me.es.osaka-u.ac.jp (F.-S. Meng).

https://doi.org/10.1016/j.commatsci.2025.113812
Received 30 November 2024; Received in revised form 5 February 2025; Accepted 25 February 2025

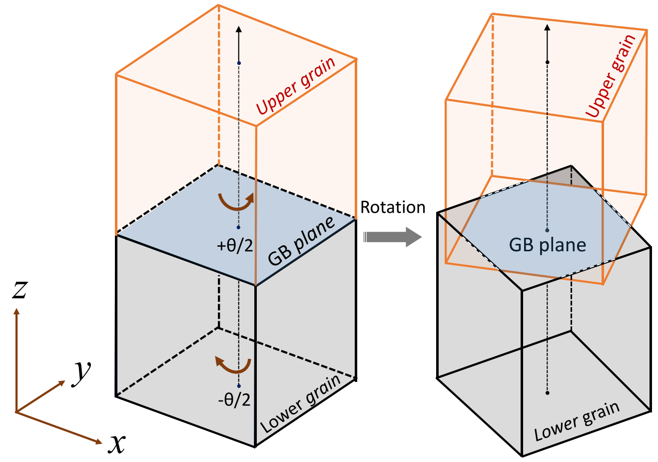

Fig. 1. Creating twist grain boundary model.

Table 1
Orientations of upper and lower grains for constructed TWGB models. *m* and *n* are positive integers (see main text).

GB plane	(001)	(110) [16]	(111)
(Upper grain) x	$[n\ m\ 0]$	$[m\ m\ \bar{n}]$	$[(m+2n)\ \overline{(2m+n)}\ (m-n)]$
(Upper grain) y	$[\bar{m}\ n\ 0]$	$[n\ n\ 2m]$	$[m\ n\ \overline{(m+n)}]$
(Lower grain) x	$[n\ \bar{m}\ 0]$	$[m\ m\ n]$	$[(2m+n)\ \overline{(m+2n)}\ (n-m)]$
(Lower grain) y	$[m\ n\ 0]$	$[\bar{n}\ \bar{n}\ 2m]$	$[n\ m\ \overline{(m+n)}]$
z	$[0\ 0\ 1]$	$[1\ \bar{1}\ 0]$	$[1\ 1\ 1]$
θ	$2\tan^{-1}(\frac{m}{n})$	$2\tan^{-1}(\frac{n}{\sqrt{2}m})$	$2\tan^{-1}(\frac{n-m}{\sqrt{3}(n+m)})$
Σ	m^2+n^2	$2m^2+n^2$	m^2+n^2+mn

systematic study of the structure and energy of (100), (110) and (111) TWGBs in α-iron at the accuracy of density functional theory (DFT) level remains conspicuously absent.

Due to the substantial number of atoms required, especially for low angle TWGBs, accurately modeling TWGB structures poses a challenge when relying on DFT-based methods. In contrast, while EIPs can handle a larger number of atoms, concerns persist regarding their accuracy and transferability [24]. Notably, Shiihara et al. [25] have recently demonstrated the capabilities of neural network interatomic potentials (NNIPs) and their superiority over EIPs in describing the structure and energy of STGBs in α-iron, using an NNIP designed for pure α-Fe [26]. As of now, machine learning interatomic potentials(MLIPs), including NNIPs, have not been applied to TWGBs.

In this paper, we conducted a comprehensive study of (001), (110), and (111) TWGBs in α-iron using our recent developed NNIP designed for the α-iron–hydrogen binary system [27]. We elucidated the relationship between GB formation energy and the twist angle in TWGBs, as well as the atomic configurations of typical dislocation networks within TWGBs featuring small twist angles. Our results were benchmarked against those derived from EAM [28] and modified EAM (MEAM) potentials [29], and were partially validated through DFT calculations. Novel 3-Dimensional (3D) dislocation networks in low angle (111) TWGBs were first uncovered and further validated using principal component analysis, an NNIP ensemble model, and other machine learning interatomic potentials for α-iron.

2. Methods

To generate (001) TWGBs, one can initiate the process from a single crystal of α-iron with a crystal orientation represented as $x[100]$, $y[010]$, and $z[001]$. Note that the x, y, and z axes are anchored to the model supercell. Subsequently, the upper and lower halves of the crystal can be rotated around the z axis by angles $\theta/2$ and -$\theta/2$ (negative angles indicate clockwise rotation, and vice versa, as illustrated in Fig. 1). When the relative rotation angle θ results in the coincidence site lattice (CSL) relationship between the upper and lower grains, the crystal orientation of the upper and lower grains can be represented as $x[nm0]$, $y[\bar{m}n0]$, $z[001]$ and $x[n\bar{m}0]$, $y[mn0]$, $z[001]$ respectively. Here, n and m are positive integers. Employing periodic boundary conditions (PBC) in the x and y directions is possible in this scenario, as the periodic units along these directions correspond to multiples of the CSL unit. The values of the twist angle θ and the CSL parameter Σ can be determined using $\theta = 2\tan^{-1}(m/n)$ and $\Sigma = (m^2 + n^2)$, respectively. Similarly, for (110) and (111) TWGBs, the grain orientations θ, and Σ can be determined, and these details are summarized in Table 1. The relative positioning of these grains along the GB plane is not uniquely determined and must be established through energy minimization analysis in actual atomic simulations.

In our atomic model, to mitigate surface effects on the prediction of energy and atomic structure of TWGBs, we adopted PBC in all directions, resulting in two equivalent TWGBs in the model. Given the capability of NNIP to handle large atomic models, a fine mesh of θ values can be employed to describe smooth θ-dependent GB energies. The GB energy (γ_{gb}) is defined as follows:

$$\gamma_{\mathrm{gb}} = (E_{\mathrm{gb}} - N\mu_{\mathrm{Fe}})/A. \tag{1}$$

In this equation, E_{gb} represents the energy of the relaxed TWGB model, and μ_{Fe} is the chemical potential of Fe atom in perfect α-iron. N and A indicate the number of Fe atoms in the TWGB model and the total area of the grain boundaries for the two GBs in the model, respectively. Prior to computing the grain boundary structure and energy, the z-dimension of the supercell shape and atomic configuration of GB model were fully relaxed. To expedite computations, we refrained from relaxing the x and y dimensions of the supercell shape, because the maximum absolute value of normal stresses in the x and y directions did not exceed 0.6 GPa, equivalent to approximately 0.2% strain.

All molecular statics simulations were carried out using LAMMPS [30] code for empirical interatomic potentials. To bridge the neural network interatomic potential and LAMMPS, an additional interface [31] was utilized. The convergence criteria during the geometric optimization relied on the atomic force that each component on any atom was no larger than 10^{-2} eV/Å. For the spin-polarized density functional theory (DFT) calculations based on the projector-augmented wave (PAW) method [32], the VASP code [33,34] was employed. The exchange–correlation functional used was the Perdew–Burke–Ernzerhof generalized gradient approximation [35]. A cutoff energy of 360 eV was chosen for the plane wave basis set, and the minimum allowed spacing between k-points was set at 0.03 Å^{-1} with a Gaussian smoothing factor of 0.1 eV. The stop condition for the electronic and ionic relaxation during the geometric optimization were set at 10^{-5} eV and 10^{-2} eV/Å, respectively.

3. Results and discussion

3.1. Comparison of fundamental properties of α-Fe from different MLIPs

To demonstrate that the NNIP employed in this study [27] is suitable for modeling the α-iron system, a systematic comparison of the fundamental properties predicted by ten previously reported machine learning interatomic potentials about α-iron, including the Gaussian Approximation Potential (GAP) [36], Artificial Neural Network potential (ANN) [26], Moment Tensor Potentials (MTPs) [37,38], Quadratic Noise Machine Learning potential (QNML) [39], Angular Depended Potential based on machine learning (ADP-ML) [40], and Deep Potentials (DPs) [41–43], has been conducted. The results are summarized in Table S1 of the supplementary materials [44]. This analysis offers essential insights into the strengths and limitations of these potentials, thereby informing their applicability across different contexts. The

NNIP exhibits good performance across most fundamental properties, with the exception of the unseen C15 cluster. In contrast, the MTP [38] and QNML [39] demonstrate promising performance in this regard. This densely packed atomic configuration is predominantly observed in nucleation radiation scenarios [45] and is less frequently associated with interfacial defects, such as GBs. Therefore, it does not present a challenge for the NNIP, which could serve as a reliable tool for the investigation of GBs.

3.2. *Grain boundary energy of* TWGBs

For the (100) TWGBs (refer to Fig. 2(a)), a total of 53 TWGBs were investigated using NNIP, covering a twist angle range from 2.794° to 43.603° with a fine twist angle mesh. The trend observed was that the GB energy increased as the twist angle increased. To assess the performance of the NNIP, the structures of four TWGBs with $\Sigma17$, $\Sigma13$, $\Sigma37$, and $\Sigma25$, having twist angles of 28.072°, 22.620°, 18.924°, and 16.260° respectively, were further relaxed using DFT calculations. The results predicted by NNIP agree well with those obtained from DFT calculations, although the NNIP slightly underestimated the GB energies. Additionally, the results obtained using the MEAM potential matched those obtained by NNIP for TWGBs with twist angles less than 10°, but then deviated from the NNIP results and approached those predicted by the EAM potential. It is noteworthy that the $\Sigma5$ GB with a twist angle of 36.870° was predicted to have the highest GB energy of 2.17 J/m^2 by NNIP, very close to the DFT results of 2.21 [27] and 2.12 J/m^2[12]. In contrast, the GB energy obtained by EAM and MEAM was 1.69 and 1.91 J/m^2, respectively.

Moving on to the (110) TWGBs (refer to Fig. 2(b)), a total of 69 TWGBs were investigated using NNIP, covering a twist angle range from 1.800° to 89.421°. The observed trend was that the GB energies increased as the twist angle increased at low twist angles, reached a plateau at twist angles of 30° to 50° with a GB energy around 0.92 J/m^2, and then a local minimum was predicted at a twist angle of 70.528° with a GB energy of 0.548 J/m^2, corresponding to the $\Sigma3$ GB. To assess the accuracy of NNIP, three TWGBs ($\Sigma9$, $\Sigma11$, and $\Sigma17$) with twist angles of 38.942°, 50.478°, and 86.628° respectively, were further relaxed using DFT calculations. The results predicted by NNIP aligned well with those obtained from our DFT calculations, as well as with previously reported DFT and tight-binding (TB) model results [12]. In the case of EIPs, there was minimal difference between results produced by EAM and MEAM, and these energy profiles were similar to the energy profile produced by NNIP, but on average had a reduction of around 30%. Interestingly, another set of reported DFT and TB model results [46] were lower than our DFT results, even lower than the EIPs results. The reason for such a disagreement among DFT calculations is unclear and certainly deserves further investigation.

Lastly, for the (111) TWGBs (refer to Fig. 2(c)), a total of 47 TWGBs were investigated using NNIP, spanning a twist angle range from 3.150° to 60.000°. To verify the performance of NNIP, three TWGBs ($\Sigma7$, $\Sigma21$, and $\Sigma3$) with twist angles of 21.787°, 38.213°, and 60.000° were further relaxed using DFT calculations, showing excellent agreement. The curve exhibits several cusps, labeled as i–iv in Fig. 2(c), and low-energy structures were identified for these points through heating the model to 600 K and then quenching it to 0 K, as indicated by the open blue squares in Fig. 2(c). The GB model represented by an open square at point iii was additionally relaxed using DFT calculations, and the GB energy was essentially not changed, as shown by the filled blue square in Fig. 2(c). Results produced by the MEAM potential were slightly lower than those obtained by the EAM potential, and both were around 20% lower than the NNIP results.

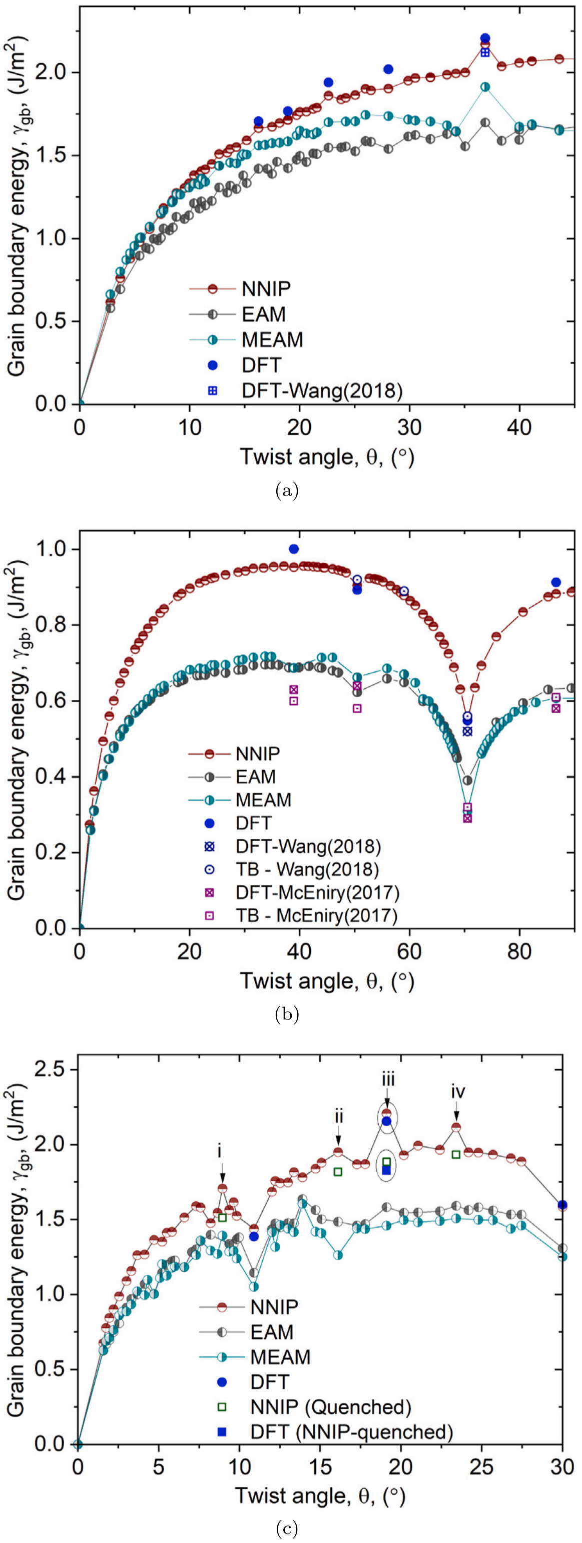

(a)

(b)

(c)

Fig. 2. GB energy (γ_{gb}) as a function of twist angle (θ) calculated using NNIP, EAM, MEAM and DFT(including the reported DFT and TB model) [12,46]. (a) for (100) TWGBs, (b) for (110) TWGBs, and (c) for (111) TWGBs. The structures are the same for the data points in the same circle in (c).

3.3. *Atomic structure of* TWGBs

Fig. 3(a) illustrates the characteristic dislocation network of (100) TWGBs. A distinct grid pattern dislocation network, comprised of two

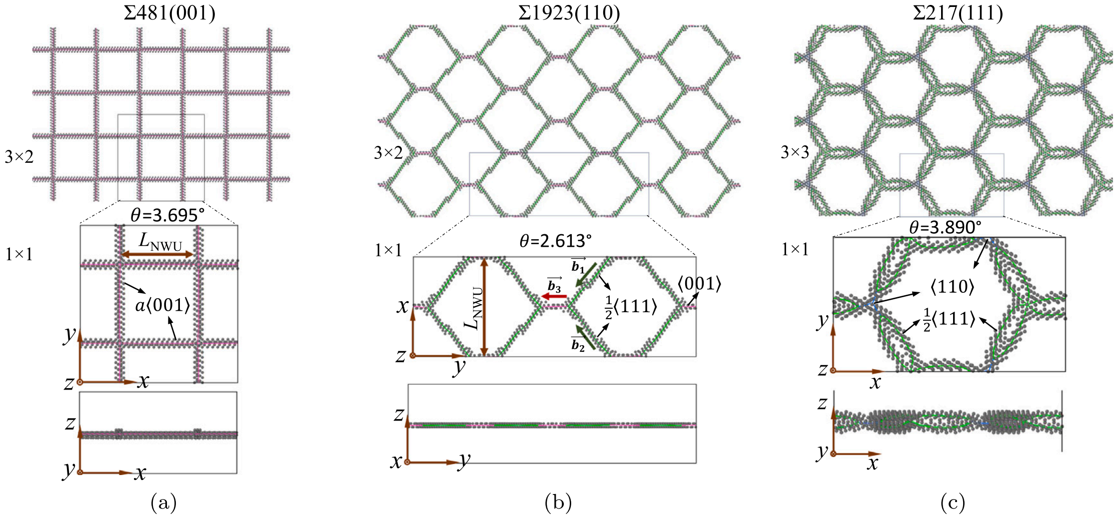

Fig. 3. Typical dislocation network for (a) (100) TWGBs, (b) (110) TWGBs, and (c) (111) TWGBs. The pink, green and blue lines in figure stands for the *a* <100>, *a*/2 <111> and *a* <110> dislocations, which are obtained via the tool of DXA [47] implemented in OVITO [48]. Fe atoms with bcc lattice are set invisible.

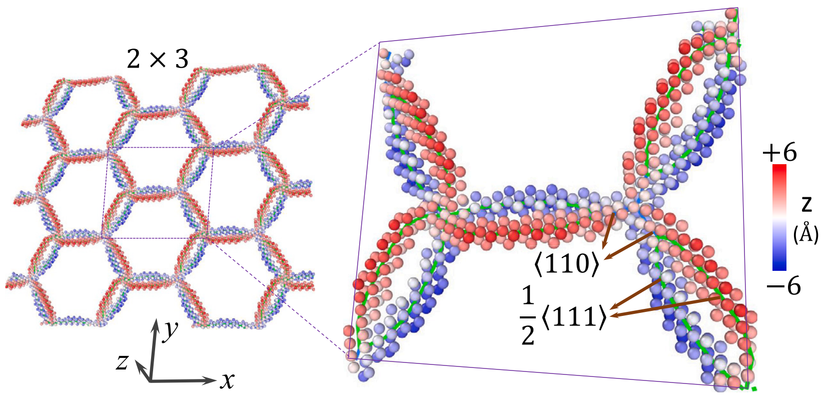

Fig. 4. Magnified view of the 3D dislocation structure of $\Sigma 217$ (111) TWGB. The green and blue lines in figure stand for the $\frac{1}{2}\langle 111\rangle$ and $\langle 110\rangle$ dislocations, which are obtained via the tool of DXA [47] implemented in OVITO [48]. Fe atoms with bcc lattice are set invisible and the remaining Fe atoms are colored by their *z* coordinates.

perpendicular $\langle 100\rangle$ screw dislocations, is prominently visible, aligning precisely with experimental findings [13]. This square network pattern persists across a broad range of twist angles. The size of the dislocation network unit, denoted as L_{NWU} in Fig. 3(a), decreases as the twist angle increases. The smallest average value of L_{NWU} we obtained is approximately 5 Å at a twist angle of 33°, marking the absence of a regular dislocation network in TWGBs beyond this angle.

In Fig. 3(b), we observe the typical dislocation network in small twist angle (110) TWGBs. It exhibits a high-density network featuring three sets of screw dislocation segments: two with $\frac{1}{2}\langle 111\rangle$ and one with $\langle 100\rangle$. This network adheres to the reaction $1/2[11\bar{1}] + 1/2[\bar{1}\bar{1}1] = [001]$ (*i.e.* , $\overrightarrow{b_1} + \overrightarrow{b_2} = \overrightarrow{b_3}$ in Fig. 3(b)) at the junction. This dislocation network pattern aligns well with experimental observations [14].

Fig. 3(c) depicts the characteristic dislocation network of (111) TWGBs with a twist angle of 3.890°. Unlike the 2-Dimensional(2D) structure of the dislocation network in (100) and (110) TWGBs, this network assumes a 3D arrangement. It comprises long $\frac{1}{2}\langle 111\rangle$ and very short $\langle 110\rangle$ dislocation segment. A magnified view of the 3D dislocation structure is presented in Fig. 4. As the twist angle increases, the prevalence of $\langle 110\rangle$ dislocations correspondingly rises. At a twist angle of 30.158°, the network is dominated by $\langle 110\rangle$ dislocations, and it vanishes at a twist angle of 32.204°, as shown in Fig.S1 in the Supplementary materials [44].

To compare the dislocation network patterns obtained using different potentials, we selected $\Sigma 481(001)$, $\Sigma 1923(110)$, and $\Sigma 217(111)$ TWGBs to represent small twist angle TWGBs with different terminations. Each configuration was relaxed using NNIP, EAM, and MEAM potentials (see Fig. 5).

All three potentials yielded identical dislocation network patterns for the (001) TWGB. Concerning the (110) TWGB, while the patterns produced by all three potentials were similar and agreed with experimental observations [14], slight differences in these patterns were discernible. Specifically, a longer $\langle 100\rangle$ dislocation correlated with a slightly larger angle α between two $\frac{1}{2}\langle 111\rangle$ dislocation segments was demonstrated in NNIP compared to EIPs. Consequently, a lower number of kinks were present in the $\frac{1}{2}\langle 111\rangle$ dislocation segments in the NNIP pattern. Notably, a significant disparity arose in the patterns for the (111) TWGB. NNIP predominantly exhibited a pattern characterized by $\frac{1}{2}\langle 111\rangle$ dislocations in a 3D spatial arrangement, whereas EAM and MEAM potentials resulted in a 2D spatial distribution dominated by $\langle 110\rangle$ dislocations. The two segments of $\frac{1}{2}\langle 111\rangle$ dislocations predicted by NNIP appeared to originate from the splitting of a single [110] dislocation seen in EIPs. This splitting, denoted as $[110] = 1/2[111] + 1/2[11\bar{1}]$, is represented as $\vec{b}_1 = \vec{b}_1^1 + \vec{b}_1^2$ in Fig. 5. This division became evident during the further relaxation of the EIPs-derived model by NNIP, as shown in the supplementary materials (Figure S2) [44]. While the reverse reaction, where two $\frac{1}{2}\langle 111\rangle$ dislocations combine to form one $\langle 110\rangle$ dislocation ($\vec{b}_1^1 + \vec{b}_1^2 = \vec{b}_1^1$), may entail higher system energy, it could be observed in systems undergoing intense plastic deformation or energetic particle irradiation [49].

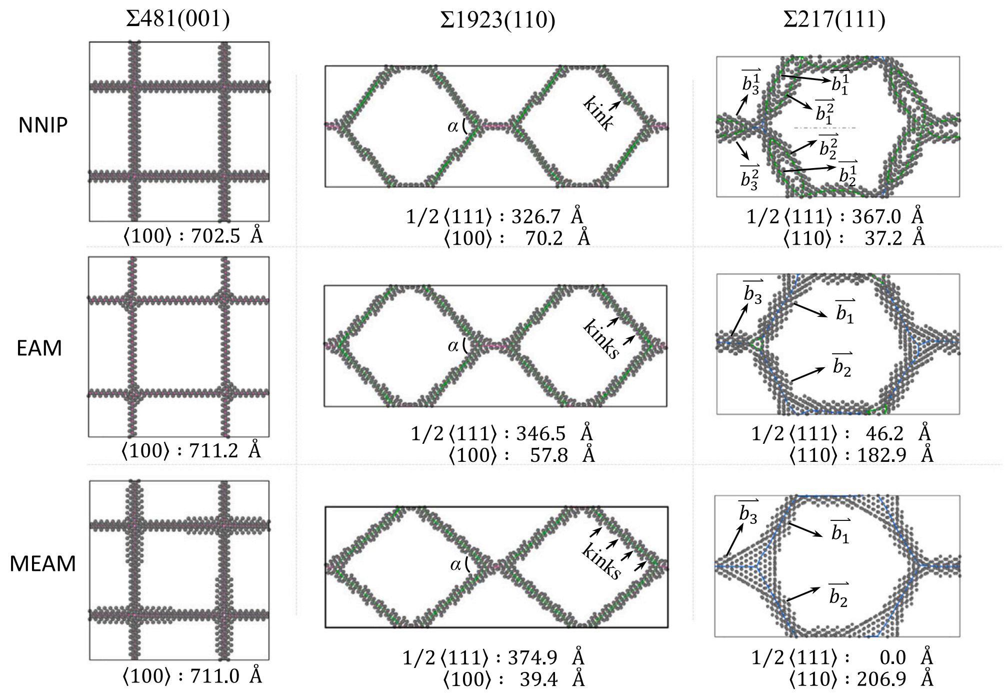

Fig. 5. Comparison of the dislocation networks of TWGBs of (100), (110), and (111) obtained by NNIP, EAM, and MEAM respectively, only show the repeated units. The pink, green and blue lines in figure stand for the ⟨100⟩, $\frac{1}{2}$⟨111⟩ and ⟨110⟩ dislocations, which are obtained via the tool of DXA [47] implemented in OVITO [48]. Fe atoms with bcc lattice are set invisible. The length of each type of dislocation for each model is printed below the figure.

3.4. *Estimation of the similarity and uncertainty of the* NNIP *for* TWGBs *with* 3D *dislocation structure*

Validating the results derived from NNIP still presents a challenge for systems beyond the computational capability of DFT calculations. As alternative solutions, one can estimate the transferability of the NNIP by similarity, i.e. compare the local atomic environments of the structures presented in simulations with those in the potential training dataset [50]. Another one is to evaluate the uncertainty of the NNIP using an ensemble model to estimate the predictive performance of the NNIP [51]. More methods for the machine-learned interatomic potentials validation please refer to a comprehensive survey in Ref. [52]. In this work, we adopted the Principal Component Analysis (PCA) [53] for similarity qualitative estimation and the ensemble model for the uncertainty quantitative estimation.

PCA is a widely adopted algorithm for reducing data dimensionality. Its primary objective is to transform k-dimensional features into p-dimensions, where these p-dimensions correspond to orthogonal features, termed principal components, providing a representation of the data in k-dimensions [54]. With the help of the structural descriptors (*i.e.*, atom centered symmetry functions, ACSF), the local atomic environments (LAEs) of atoms in the dataset used in the NNIP training were transferred to a matrix $\chi_{m\times n}$, where m and n stand for the number of LAEs in the database and number of ACSFs of each atom. The type and hyper parameters of the structural descriptors were the same as in the NNIP training [27]. To simplify the analysis, all datasets with H atoms and structural descriptors including H atoms were excluded. The size of the obtained $\chi_{m\times n}$ is (1 424 768 × 24). The PCA results are shown in Fig. 6(a), where the data points are colored according to their respective structural types. The LAEs of atoms in Σ217(111) TWGB with 3D dislocation network (marked as 3D-twist in Fig. 6(a)) are entirely within the region of the LAEs derived from the training dataset, which means that the obtained 3D structure was from the interpolation rather than exploration of the NNIP.

Using the same neural network architecture and database, twelve NNIPs (labeled NNIP-i, i = 1–12) were newly trained. A unique random number seed was assigned to each training task, which was used to the random separation of the database into training and testing datasets, while all other settings were kept. Each of the NNIP was trained with fixed 160 iterations. We took the root mean squared error (RMSE) of energy and force as the overall accuracy. RMSEs of energy across all 12 NNIPs are in a range of 3.47–5.43 and 3.46–10.33 meV/atom in the training and testing dataset, respectively. RSMEs of force are 0.077–0.083 and 0.077–0.145 eV/Å in the training and testing dataset. The energy RMSE of NNIP-5 and force RMSE of NNIP-12 in the testing dataset are larger than others. This kind of exception is frequently engaged in the NNIPs training process [55]. Details of RMSEs for each NNIP are tabulated in Table.S2 in the supplementary materials [44].

A TWGB of Σ217(111) was used to estimate the uncertainty of the NNIP. The structure of the TWGB was examined using these 12 NNIPs. All new NNIPs predicted the similar 3D dislocation network in the TWGB (See Fig.S3 in the supplementary materials [44]). The common presence of the typical atomic structure from the ensemble of NNIP may serve as evidence that the local atomic environments of the 3D dislocation network have been included in the database. With the help of Eq. (1), the γ_{gb} from each NNIP was computed based on their own produced lattice constant and chemical potential of perfect α-Fe (see Table.S2 in supplementary materials [44]). The γ_{gb}s are in a small range of 0.8348–0.8635 J/m^2. The variance of γ^K_{gb} from NNIP-K can be determined by:

$$\sigma^K_{\gamma_{\text{gb}}} = \sqrt{\frac{1}{N}\sum_{i=0}^{n}(\gamma^i_{\text{gb}} - \gamma^K_{\text{gb}})^2},\quad n = 12 \tag{2}$$

where, N is the number of NNIPs, i.e., N = 13. γ^0_{gb} is from the primary NNIP used in this work. The values of $\sigma_{\gamma_{\text{gb}}}$ obtained are no more than 0.02 J/m^2. The GB energy from each NNIP together with the corresponding RMSE are plotted in Fig. 6(b). This result indicates the low uncertainty and high reliability of the NNIP.

The force uncertainty was also estimated for the model of Σ217(111) TWGB from NNIP-0. The averaged atomic force RMSE is about 10 meV/Å, which aligns closely with the typical DFT force convergence criteria of 0.01 eV/Å during the NNIP database generation,

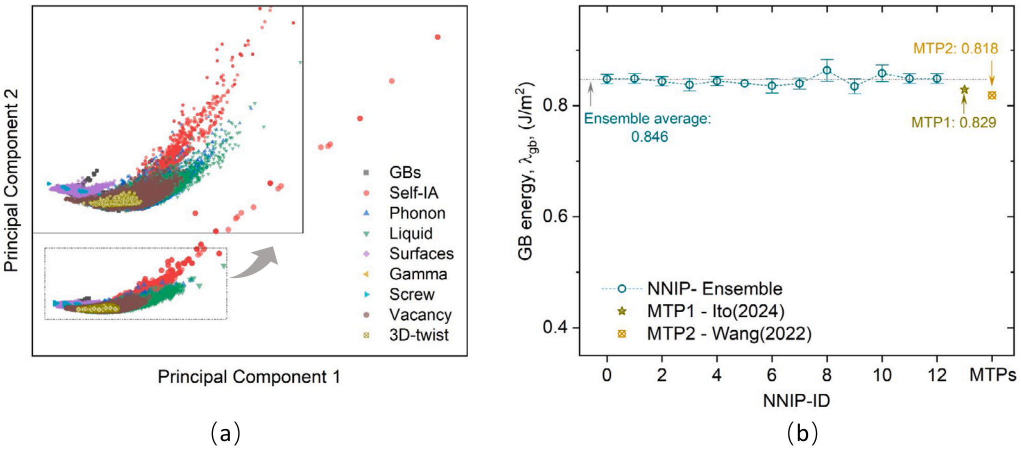

(a) (b)

Fig. 6. (a) PCA for the dataset used in the NNIP training and the Σ217(111) TWGB obtained by NNIP-0. All data points are colored according to the structure type. Self-IA stands for the self interstitial atoms. The inset panel presents a magnified view of the area enclosed by the dotted rectangle. (b) GB energy and their RMSE for the model of Σ217(111) TWGB predicted by all NNIPs. NNIP-0 is the primary NNIP used in this work. The raw data can be found in the supplementary materials (Table. S2) [44]. Results from MTPs prediction [37,38] is also printed.

evidencing low uncertainty and high reliability of NNIP. Details please refer to the supplementary materials (Table. S3) [44].

3.5. Discussion

The 3D dislocation network uncovered in this work might have significant effects on the mechanical property of metals. Firstly, in contrast to the movable 2D hexagonal dislocation network in (110) TWGBs in bcc metals [14,20], the mobility of the entire 3D dislocation network in (111) TWGBs is expected to be constrained due to the involvement of multiple slip systems and complex dislocation interactions. This restriction might have impact on the toughness of the metals. Secondly, these 3D dislocation networks can be regarded as pre-existing dislocations within materials. The activation stress of a single pre-existing dislocation is expected to be lower than that of newly formed dislocations, and their motion may help to relieve deformation-induced stress, thereby improving the material's plasticity. Thirdly, the length of the dislocation line in the 3D case is roughly double that in the 2D case. This suggests that the 3D dislocation network may trap a greater number of interstitial atoms (H, C, N, O, ...) leading to change of GB mechanical property [4,56]. Finally, the micro-defects might have effects on GB mechanical property, and the NNIP could handle such kind of interactions due to its good performance in the description of various defects [27].

Partial 3D dislocation networks from EIPs were presented in (111) TWGBs with very small twist angles (see Fig. S4 in the supplementary materials [44]). We believe that the fundamental reason for the difference in the dislocation network of (111) TWGBs between 3D from NNIP and 2D from EIPs lies in the performance of interatomic potentials for different types of dislocations, i.e. the dislocation stability competition in the dislocation reaction of $[110] = 1/2[111] + 1/2[11\bar{1}]$. A cross-verification of the 3D dislocation network in Σ217(111) TWGB was conducted using two machine-learning-based MTPs with DFT accuracy deigned for general GBs [37] and radiation damage effects [38] in α-iron. The GB energies obtained are 0.829 and 0.818 J/m^2 respectively, and the similar 3D dislocation network was obtained, the results are provided in Fig. S5 of the supplementary materials [44]. Given the high accuracy of the NNIP in describing the energetics of dislocations [27], it is expected to provide a more precise depiction of the reaction compared to EIPs. This reaction might change its direction due to external effects, such as temperatures, deformation, *etc*.. Since the accurate description of interfacial dislocations is vital for understanding the physical and mechanical properties of interfaces [57], we anticipate that our theoretical predictions will inspire experimental researchers, whose future observations may provide validation for our findings.

4. Conclusion

In summary, our investigation delved into the energy and atomic structure of (100), (110), and (111) twist grain boundaries (TWGBs) in α-iron employing Fe–H NNIP and, for certain cases were supplemented with DFT calculations. The key findings can be summarized as follows:

We meticulously charted the grain boundary energy of TWGBs across a wide spectrum of twist angles for (100), (110), and (111) terminations, remarkably achieving concordance between NNIP predictions and DFT calculations. Notably, the results obtained by EIPs stood approximately 20% to 30% lower than those by NNIP.

Exploring dislocation networks in TWGBs with small twist angles unraveled distinct network patterns. For (100) TWGBs, the network adopted a grid pattern, constituted by perpendicular $\langle 100\rangle$ screw dislocations. In the case of (110) TWGBs, a hexagonal network pattern emerged, mirroring experimental observations in BCC metals. This pattern encompassed two segments of $1/2\langle 111\rangle$ and one of $\langle 110\rangle$ dislocations. Significantly, (111) TWGBs with small twist angles exhibited a novel 3D dislocation pattern primarily composed of $1/2\langle 111\rangle$ dislocations, a phenomenon uncovered for the first time. The novel 3D dislocation pattern was validated through principal component analysis, NNIP ensemble model, and further crossing verification using two independent machine learning based MTPs respectively designed for general GBs and radiation damage effects in α-iron. The varying performance of various interatomic potentials in evaluating the stability of various types of dislocations influences the type of dislocation networks in (111) small-angle TWGBs.

In essence, our study has illuminated the nuanced energetics and structural intricacies characterizing various TWGB orientations in α-iron, highlighting the remarkable predictive power of NNIP and shedding light on the uncharted territories of dislocation networks in certain configurations.

CRediT authorship contribution statement

Fan-Shun Meng: Writing – original draft, Validation, Methodology, Investigation, Conceptualization. **Jiu-Hui Li:** Investigation. **Shuhei Shinzato:** Validation, Methodology, Investigation, Conceptualization. **Kazuki Matsubara:** Validation, Investigation. **Wen-Tong Geng:** Writing – review & editing, Resources, Conceptualization. **Shigenobu Ogata:** Writing – review & editing, Supervision, Resources, Project administration.

Declaration of competing interest

The authors declare that they have no known competing financial interests or personal relationships that could have appeared to influence the work reported in this paper.

Acknowledgments

J.-H. L. thanks to the financial support from the Liaoning Provincial Natural Science Foundation of China (Grant No. 2020-BS-241). F.-S. M. and S.O. acknowledge the support by JFE Steel Corporation, Japan, and the Elements Strategy Initiative for Structural Materials (ESISM), Japan. W.-T.G. was supported by National Key R&D Program of China (Grant No. 2022YFB3707501). S.O. acknowledges the support by JSPS KAKENHI (Grant Nos. JP23H00161 and JP23K20037), and the supported by MEXT (Ministry of Education, Culture, Sport, Science and Technology of Japan) Programs (Grant Nos. JPMXP1122684766, JPMXP1020230325, and JPMXP1020230327). Part of calculations were performed using computational resources of supercomputer Fugaku provided by the RIKEN Center for Computational Science (Project IDs: hp230205, hp240224 and hp230212), the large-scale computer systems at the Cybermedia Center, Osaka University, and the Large-scale parallel computing server at the Center for Computational Materials Science, Institute for Materials Research, Tohoku University.

Appendix A. Supplementary data

Supplementary material related to this article can be found online at https://doi.org/10.1016/j.commatsci.2025.113812.

Data availability

The primary NNIP used in this study can be found at: https://www.ctcms.nist.gov/potentials/entry 2021–Meng-F-S-Du-J-P-Shinzato-S-et-al–Fe-H, and the newly trained 12 NNIPs in ensemble can be found at: https://github.com/mengfsou/FeH-NNIP-ensemble.

References

[1] K. Lu, Making strong nanomaterials ductile with gradients, Science 345 (6203) (2014) 1455–1456, http://dx.doi.org/10.1126/science.1255940.

[2] M. Všianská, M. Šob, The effect of segregated sp-impurities on grain-boundary and surface structure, magnetism and embrittlement in nickel, Prog. Mater. Sci. 56 (6) (2011) 817–840, http://dx.doi.org/10.1016/j.pmatsci.2011.01.008.

[3] I.J. Beyerlein, M.J. Demkowicz, A. Misra, B. Uberuaga, Defect-interface interactions, Prog. Mater. Sci. 74 (2015) 125–210, http://dx.doi.org/10.1016/j.pmatsci.2015.02.001.

[4] K. Song, S. Cao, Y. Bao, P. Qian, Y. Su, Designing hydrogen embrittlement-resistant grain boundary in steel by alloying elements segregation: First-principles calculations, Appl. Surf. Sci. 656 (2024) 159684, http://dx.doi.org/10.1016/j.apsusc.2024.159684.

[5] M.A. Tschopp, K. Solanki, F. Gao, X. Sun, M.A. Khaleel, M. Horstemeyer, Probing grain boundary sink strength at the nanoscale: Energetics and length scales of vacancy and interstitial absorption by grain boundaries in α-Fe, Phys. Rev. B 85 (6) (2012) 064108, http://dx.doi.org/10.1103/PhysRevB.85.064108.

[6] D. Qiu, P. Zhao, C. Shen, W. Lu, D. Zhang, M. Mrovec, Y. Wang, Predicting grain boundary structure and energy in bcc metals by integrated atomistic and phase-field modeling, Acta Mater. 164 (2019) 799–809, http://dx.doi.org/10.1016/j.actamat.2018.11.023.

[7] H. Zheng, X.-G. Li, R. Tran, C. Chen, M. Horton, D. Winston, K.A. Persson, S.P. Ong, Grain boundary properties of elemental metals, Acta Mater. 186 (2020) 40–49, http://dx.doi.org/10.1016/j.actamat.2019.12.030.

[8] O. Chirayutthanasak, R. Sarochawikasit, S. Khongpia, T. Okita, S. Dangtip, G.S. Rohrer, S. Ratanaphan, Universal function for grain boundary energies in bcc metals, Scr. Mater. 240 (2024) 115821, http://dx.doi.org/10.1016/j.scriptamat.2023.115821.

[9] K. Ito, Significant effect of magnetism on grain boundary segregation in γ-Fe: A systematic comparison of grain boundary segregation in nonmagnetic and paramagnetic γ-Fe by first-principles calculations, Mater. Today Commun. 38 (2024) 107849, http://dx.doi.org/10.1016/j.mtcomm.2023.107849.

[10] P. Lejček, M. Šob, Entropy: A controversy between experiment and calculations in grain boundary segregation, Prog. Mater. Sci. (2025) 101431, http://dx.doi.org/10.1016/j.pmatsci.2025.101431.

[11] J.-M. Zhang, Y.-H. Huang, X.-J. Wu, K.-W. Xu, Energy calculation for symmetrical tilt grain boundaries in iron, Appl. Surf. Sci. 252 (14) (2006) 4936–4942, http://dx.doi.org/10.1016/j.apsusc.2005.07.046.

[12] J. Wang, G.K. Madsen, R. Drautz, Grain boundaries in bcc-Fe: A density-functional theory and tight-binding study, Modelling Simul. Mater. Sci. Eng. 26 (2) (2018) 025008, http://dx.doi.org/10.1088/1361-651X/aa9f81.

[13] K.E. Sickafus, S. Sass, Grain boundary structural transformations induced by solute segregation, Acta Metall. 35 (1) (1987) 69–79, http://dx.doi.org/10.1016/0001-6160(87)90214-8.

[14] S. Ohr, D. Beshers, Crystallography of dislocation networks in annealed iron, Phil. Mag. 8 (92) (1963) 1343–1360, http://dx.doi.org/10.1080/14786436308207298.

[15] J. Hetherly, E. Martinez, M. Nastasi, A. Caro, Helium bubble growth at BCC twist grain boundaries, J. Nucl. Mater. 419 (2011) 201–207, http://dx.doi.org/10.1016/j.jnucmat.2011.08.009.

[16] J. Yang, Y. Nagai, M. Hasegawa, Y.N. Osetsky, Atomic scale modeling of $\{110\}$ twist grain boundaries in α-iron: Structure and energy properties, Phil. Mag. 90 (7–8) (2010) 991–1000, http://dx.doi.org/10.1080/14786430903154086.

[17] Z.-H. Liu, Y.-X. Feng, J.-X. Shang, Characterizing twist grain boundaries in BCC Nb by molecular simulation: Structure and shear deformation, Appl. Surf. Sci. 370 (2016) 19–24, http://dx.doi.org/10.1016/j.apsusc.2016.02.097.

[18] Y.-X. Feng, J.-X. Shang, Z.-H. Liu, G.-H. Lu, The energy and structure of (1 1 0) twist grain boundary in tungsten, Appl. Surf. Sci. 357 (2015) 262–267, http://dx.doi.org/10.1016/j.apsusc.2015.08.265.

[19] H. Kurishita, S. Kuba, H. Kubo, H. Yoshinaga, Misorientation dependence of grain boundary fracture in molybdenum bicrystals with various $\langle 110 \rangle$ twist boundaries, Trans. Japan Inst. Met. 26 (5) (1985) 332–340, http://dx.doi.org/10.2320/matertrans1960.26.332.

[20] J. Yang, Y. Osetsky, R. Stoller, Y. Nagai, M. Hasegawa, The effect of twist angle on anisotropic mobility of $\{110\}$ hexagonal dislocation networks in α-iron, Scr. Mater. 66 (10) (2012) 761–764, http://dx.doi.org/10.1016/j.scriptamat.2012.01.061.

[21] R. Sarochawikasit, C. Wang, P. Kumam, H. Beladi, T. Okita, G.S. Rohrer, S. Ratanaphan, Grain boundary energy function for α iron, Materialia 19 (2021) 101186, http://dx.doi.org/10.1016/j.mtla.2021.101186.

[22] G. Liu, Z. Qiu, Y. Xie, Y. Wang, D. Leng, X. Tian, Dislocation evaluation of Fe twist grain boundary based on molecular dynamics, J. Nanosci. Nanotechnol. 19 (2019) 729–742, http://dx.doi.org/10.1166/jnn.2018.15898.

[23] M. Wakeda, T. Ohmura, Atomistic evaluation of the dislocation transmission across tilt and twist low-angle grain boundaries in body-centered cubic iron, Comput. Mater. Sci. 228 (2023) 112335, http://dx.doi.org/10.1016/j.commatsci.2023.112335.

[24] G.P. Pun, R. Batra, R. Ramprasad, Y. Mishin, Physically informed artificial neural networks for atomistic modeling of materials, Nat. Commun. 10 (1) (2019) 2339, http://dx.doi.org/10.1038/s41467-019-10343-5.

[25] Y. Shiihara, R. Kanazawa, D. Matsunaka, I. Lobzenko, T. Tsuru, M. Kohyama, H. Mori, Artificial neural network molecular mechanics of iron grain boundaries, Scr. Mater. 207 (2022) 114268, http://dx.doi.org/10.1016/j.scriptamat.2021.114268.

[26] H. Mori, T. Ozaki, Neural network atomic potential to investigate the dislocation dynamics in bcc iron, Phys. Rev. Mater. 4 (4) (2020) 040601, http://dx.doi.org/10.1103/PhysRevMaterials.4.040601.

[27] F.-S. Meng, J.-P. Du, S. Shinzato, H. Mori, P. Yu, K. Matsubara, N. Ishikawa, S. Ogata, General-purpose neural network interatomic potential for the α-iron and hydrogen binary system: Toward atomic-scale understanding of hydrogen embrittlement, Phys. Rev. Mater. 5 (11) (2021) 113606, http://dx.doi.org/10.1103/PhysRevMaterials.5.113606.

[28] M. Wen, A new interatomic potential describing Fe-H and H–H interactions in bcc iron, Comput. Mater. Sci. 197 (2021) 110640, http://dx.doi.org/10.1016/j.commatsci.2021.110640.

[29] B.-J. Lee, J.-W. Jang, A modified embedded-atom method interatomic potential for the Fe–H system, Acta Mater. 55 (20) (2007) 6779–6788, http://dx.doi.org/10.1016/j.actamat.2007.08.041.

[30] A.P. Thompson, H.M. Aktulga, R. Berger, D.S. Bolintineanu, W.M. Brown, P.S. Crozier, P.J. in't Veld, A. Kohlmeyer, S.G. Moore, T.D. Nguyen, et al., Lammps-a flexible simulation tool for particle-based materials modeling at the atomic, meso, and continuum scales, Comput. Phys. Comm. 271 (2022) 108171, http://dx.doi.org/10.1016/j.cpc.2021.108171.

[31] A. Singraber, J. Behler, C. Dellago, Library-based lammps implementation of high-dimensional neural network potentials, J. Chem. Theory Comput. 15 (3) (2019) 1827–1840, http://dx.doi.org/10.1021/acs.jctc.8b00770.

[32] G. Kresse, D. Joubert, From ultrasoft pseudopotentials to the projector augmented-wave method, Phys. Rev. B 59 (3) (1999) 1758, http://dx.doi.org/10.1103/PhysRevB.59.1758.

[33] G. Kresse, J. Furthmüller, Efficiency of ab-initio total energy calculations for metals and semiconductors using a plane-wave basis set, Comput. Mater. Sci. 6 (1) (1996) 15–50, http://dx.doi.org/10.1016/0927-0256(96)00008-0.

[34] G. Kresse, J. Furthmüller, Efficient iterative schemes for ab initio total-energy calculations using a plane-wave basis set, Phys. Rev. B 54 (16) (1996) 11169, http://dx.doi.org/10.1103/PhysRevB.54.11169.

[35] J.P. Perdew, K. Burke, M. Ernzerhof, Generalized gradient approximation made simple, Phys. Rev. Lett. 77 (18) (1996) 3865, http://dx.doi.org/10.1103/PhysRevLett.77.3865.

[36] D. Dragoni, T.D. Daff, G. Csányi, N. Marzari, Achieving DFT accuracy with a machine-learning interatomic potential: Thermomechanics and defects in bcc ferromagnetic iron, Phys. Rev. Mater. 2 (1) (2018) 013808, http://dx.doi.org/10.1103/PhysRevMaterials.2.013808.

[37] K. Ito, T. Yokoi, K. Hyodo, H. Mori, Machine learning interatomic potential with DFT accuracy for general grain boundaries: Analysis of grain boundary energy and atomic structure in α-Fe polycrystals, Npj Comput. Mater. 10 (2024) 255, http://dx.doi.org/10.1038/s41524-024-01451-y.

[38] Y. Wang, J. Liu, J. Li, J. Mei, Z. Li, W. Lai, F. Xue, Machine-learning interatomic potential for radiation damage effects in bcc-iron, Comput. Mater. Sci. 202 (2022) 110960, http://dx.doi.org/10.1016/j.commatsci.2021.110960.

[39] A.M. Goryaeva, J. Dérès, C. Lapointe, P. Grigorev, T.D. Swinburne, J.R. Kermode, L. Ventelon, J. Baima, M.-C. Marinica, Efficient and transferable machine learning potentials for the simulation of crystal defects in bcc Fe and W, Phys. Rev. Mater. 5 (10) (2021) 103803, http://dx.doi.org/10.1103/PhysRevMaterials.5.103803.

[40] S. Starikov, D. Smirnova, T. Pradhan, Y. Lysogorskiy, H. Chapman, M. Mrovec, R. Drautz, Angular-dependent interatomic potential for large-scale atomistic simulation of iron: Development and comprehensive comparison with existing interatomic models, Phys. Rev. Mater. 5 (6) (2021) 063607, http://dx.doi.org/10.1103/PhysRevMaterials.5.063607.

[41] F.-S. Meng, S. Shinzato, S. Zhang, K. Matsubara, J.-P. Du, P. Yu, W.-T. Geng, S. Ogata, A highly transferable and efficient machine learning interatomic potentials study of α-Fe–C binary system, Acta Mater. 281 (2024) 120408, http://dx.doi.org/10.1016/j.actamat.2024.120408.

[42] F. Wu, Z. Liu, Y. Chen, X. Guo, J. Xue, Y. Li, H. Huang, H. Zhou, H. Deng, Deep learning-based neural network potential for investigating the synergistic effect of H and He in bcc-Fe, Comput. Mater. Sci. 246 (2025) 113434, http://dx.doi.org/10.1016/j.commatsci.2024.113434.

[43] K.C. Pitike, W. Setyawan, Accurate Fe–He machine learning potential for studying He effects in bcc-Fe, J. Nucl. Mater. 574 (2023) 154183, http://dx.doi.org/10.1016/j.jnucmat.2022.154183.

[44] please see the supplementary document of Formation of Three-Dimensional Dislocation Networks in α-Iron Twist Grain Boundaries: Insights from First-Principles Neural Network Interatomic Potentials in Appendix A.

[45] J. Byggmästar, F. Granberg, Dynamical stability of radiation-induced C15 clusters in iron, J. Nucl. Mater. 528 (2020) 151893, http://dx.doi.org/10.1016/j.jnucmat.2019.151893.

[46] E.J. McEniry, T. Hickel, J. Neugebauer, Hydrogen behaviour at twist $\{110\}$ grain boundaries in α-Fe, Philos. Trans. R. Soc. A: Math. Phys. Eng. Sci. 375 (2098) (2017) 20160402, http://dx.doi.org/10.1098/rsta.2016.0402.

[47] A. Stukowski, K. Albe, Extracting dislocations and non-dislocation crystal defects from atomistic simulation data, Modelling Simul. Mater. Sci. Eng. 18 (8) (2010) 085001, http://dx.doi.org/10.1088/0965-0393/18/8/085001.

[48] A. Stukowski, Visualization and analysis of atomistic simulation data with ovito–the open visualization tool, Modelling Simul. Mater. Sci. Eng. 18 (1) (2009) 015012, http://dx.doi.org/10.1088/0965-0393/18/1/015012.

[49] K. Arakawa, T. Amino, H. Yasuda, H. Mori, $\langle 110\rangle$ dislocation junction formation via the coalescence between nanoscale $1/2\langle 111\rangle$ prismatic dislocation loops in iron, ISIJ Int. 57 (11) (2017) 2065–2069, http://dx.doi.org/10.2355/isijinternational.ISIJINT-2017-173.

[50] J.S. Smith, B. Nebgen, N. Mathew, J. Chen, N. Lubbers, L. Burakovsky, S. Tretiak, H.A. Nam, T. Germann, S. Fensin, et al., Automated discovery of a robust interatomic potential for aluminum, Nat. Commun. 12 (1) (2021) 1257, http://dx.doi.org/10.1038/s41467-021-21376-0.

[51] K. Tran, W. Neiswanger, J. Yoon, Q. Zhang, E. Xing, Z.W. Ulissi, Methods for comparing uncertainty quantifications for material property predictions, Mach. Learn.: Sci. Technol. 1 (2) (2020) 025006, http://dx.doi.org/10.1088/2632-2153/ab7e1a.

[52] J.D. Morrow, J.L. Gardner, V.L. Deringer, How to validate machine-learned interatomic potentials, J. Chem. Phys. 158 (12) (2023) http://dx.doi.org/10.1063/5.0139611.

[53] H. Abdi, L.J. Williams, Principal component analysis, Wiley Interdiscip. Rev.: Comput. Stat. 2 (4) (2022) 433–459, http://dx.doi.org/10.1002/wics.101.

[54] Y. You, D. Zhang, F. Wu, X. Cao, Y. Sun, Z.-Z. Zhu, S. Wu, Principal component analysis enables the design of deep learning potential precisely capturing LLZO phase transitions, Npj Comput. Mater. 10 (1) (2024) 57, http://dx.doi.org/10.1038/s41524-024-01240-7.

[55] D. Marchand, W. Curtin, Machine learning for metallurgy IV: A neural network potential for Al-Cu-Mg and Al-Cu-Mg-Zn, Phys. Rev. Mater. 6 (5) (2022) 053803, http://dx.doi.org/10.1103/PhysRevMaterials.6.053803.

[56] A. Shibata, I. Gutierrez-Urrutia, A. Nakamura, T. Moronaga, K. Okada, Y. Madi, J. Besson, T. Hara, Local crack arrestability and deformation microstructure evolution of hydrogen-related fracture in martensitic steel, Corros. Sci. 233 (2024) 112092, http://dx.doi.org/10.1016/j.corsci.2024.112092.

[57] J.-Y. Zhang, Y. Gao, Y. Wang, W.-Z. Zhang, A generalized O-element approach for analyzing interface structures, Acta Mater. 165 (2019) 508–519, http://dx.doi.org/10.1016/j.actamat.2018.12.005.